

# A photoionization model of the spatial distribution of the optical and mid-IR properties in NGC 595

E. Pérez-Montero<sup>1</sup>, M. Relaño<sup>2</sup>, J. M. Vílchez<sup>1</sup> & A. Monreal-Ibero<sup>1,3</sup>

<sup>1</sup> *Instituto de Astrofísica de Andalucía. CSIC. Apartado de correos 3004. 18080, Granada, Spain.*

<sup>2</sup> *Institute of Astronomy. University of Cambridge, Madingley Road, Cambridge, CB3 0HA, UK*

<sup>3</sup> *Astrophysikalisches Institut Postdam, An der Sternwarte 16, 14482 Postdam, Germany*

Accepted Received ; in original form November 2006

## ABSTRACT

We present a set of photoionization models that reproduce simultaneously the observed optical and mid-infrared spatial distribution of the H II region NGC 595 in the disk of M33 using the code CLOUDY. Both optical (PMAS-Integral Field Spectroscopy) and mid-infrared ( $8\ \mu\text{m}$  and  $24\ \mu\text{m}$  bands from Spitzer) data provide enough spatial resolution to model in a novel approach the inner structure of the H II region. We define a set of elliptical annular regions around the central ionizing cluster with an uniformity in their observed properties and consider each annulus as an independent thin shell structure. For the first time our models fit the relative surface brightness profiles in both the optical ( $\text{H}\alpha$ ,  $[\text{O II}]$ ,  $[\text{O III}]$ ) and the mid-infrared emissions ( $8\ \mu\text{m}$  and  $24\ \mu\text{m}$ ), under the assumption of a uniform metallicity ( $12+\log(\text{O}/\text{H}) = 8.45$ ; Esteban et al. 2009) and an age for the stellar cluster of 4.5 Myr (Malumuth et al. 1996). Our models also reproduce the observed uniformity of the  $R_{23}$  parameter and the increase of the  $[\text{O II}]/[\text{O III}]$  ratio due to the decrease of the ionization parameter. The variation of the  $\text{H}\alpha$  profile is explained in terms of the differences of the occupied volume (the product of filling factor and total volume of the shell) in a matter-bounded geometry, which also allows to reproduce the observed pattern of the extinction. The  $8\ \mu\text{m}/24\ \mu\text{m}$  ratio is low (ranging between 0.04 and 0.4) because it is dominated by the surviving of small dust grains in the H II region, while the PAHs emit more weakly because they cannot be formed in these thin H II gas shells. The ratio is also well fitted in our models by assuming a dust-to-gas ratio in each annulus compatible with the integrated estimate for the whole H II region after the  $70\ \mu\text{m}$  and  $160\ \mu\text{m}$  Spitzer observations.

**Key words:** ISM: H II regions, dust, extinction, abundances – galaxies : individual : M33

## 1 INTRODUCTION

The approach to study the physical properties of H II regions is changing nowadays with the availability of spectroscopic observations covering the whole face of these objects. The observations are normally done with Integral Field Spectroscopy (IFS) instruments such as PMAS (*Potsdam Multi Aperture Spectrophotometer*, Sánchez, Cardiel & Verheijen et al. 2007), VIMOS (Le Fèvre et al., 2003), and others. These observations present a challenge for the classical photoionization models, which have normally been applied to explain long-slit observations typically centered at the location of the most intense knots within the regions. 3D photoionization models allow the simulation of the thermal and ionization structure in different geometries assuming different distributions for the ionizing sources. Using these techniques Wood et al. (2004) studied the variation of the emis-

sion line intensities in a stratified structure, with an increase of the temperature and the ratios involving low excitation ions, like  $[\text{N II}]/\text{H}\alpha$  or  $[\text{S II}]/\text{H}\alpha$ . More recently, 3D photoionization models of H II regions show that some of the physical parameters normally assumed to be constant are influenced by the configuration of the stars and gas within the region (Ercolano, Bastian & Stasińska 2007). Nevertheless, the most important constraint to this approach is the assumed symmetry of the gas configuration in the models. This approach can hardly be applied when comparing with IFS-based data, given the complex structure of most GHI-IRs, mainly due to the interplay between the stars, gas and dust.

In a recent paper, Relaño et al. (2010) presented IFS observations of NGC 595, covering the major fraction of its surface. These authors created maps of the main emission lines observed within the 3650-6990 Å spectral range

and study the variations of the physical properties across the surface of the region. The  $[\text{S II}]\lambda 6717/[\text{S II}]\lambda 6731$  emission line ratio map, tracing the electron density, does not show any relevant structure, but the  $[\text{S II}]\lambda 6717,6731/\text{H}\alpha$ ,  $[\text{N II}]\lambda 6584/\text{H}\alpha$ ,  $[\text{O III}]\lambda 5007/\text{H}\beta$  maps nicely depict the ionization structure of the region. They also obtain a reddening map whose maximum correlates well with the maximum of the  $24\ \mu\text{m}$  emission, showing that the dust emitting at this wavelength band is probably mixed with the ionized gas of the region and heated by the central ionizing stars. The authors also study the variation of several classical emission line ratios proposed as metallicity tracers and find that while the  $R_{23}$  index (Pagel et al. 1979) varies slightly within the region,  $[\text{N II}]/\text{H}\alpha$  and  $[\text{N II}]/[\text{O III}]$  show significant variations across the surface of NGC 595.

Here, we present new photoionization models of NGC 595 in order to explain the results of the 3D spectroscopic observations performed by Relaño et al. (2010) as well as the recently observed spatial distribution of the IR emission. Due to its size and revealed shell structure, NGC 595 is a very suitable object to apply photoionization models. It is the second most luminous H II region in M33 and presents an angular size of  $\sim 1'$ , corresponding to a linear physical size of  $\sim 250\ \text{pc}$ <sup>\*</sup>. The region has an H $\alpha$  shell morphology that shows the action of the stellar winds of the massive stars located in its interior. Its age,  $4.5 \pm 1.0\ \text{Myr}$ , was previously estimated by stellar photometry (Malumuth, Waller, & Parker 1996) and by synthesis of integrated spectra in the far-ultraviolet (FUV) wavelength range (Pellerin 2006). The stellar content of the H II region is made of  $\sim 250$  OB-type stars,  $\sim 13$  supergiants (Malumuth et al. 1996) and 9 spectroscopically confirmed Wolf-Rayet (WR) stars (Drissen et al. 2008), plus a new WR star discovered using IFS (Relaño et al. 2010) and located farther away from the other WR stars. The physical properties for NGC 595 were also derived using long-slit spectroscopic observations (Vílchez et al. 1988) and echelle spectroscopy (Esteban et al. 2009). The electron temperature of the region is  $\sim 8000\ \text{K}$ , the electron density is consistent with the low density limit, and the estimated metallicity range is  $12 + \log[\text{O}/\text{H}] = 8.4\text{--}8.6$ , depending on the authors and the observational technique to derive it (Vílchez et al. 1988; Esteban et al. 2009; Relaño et al. 2010).

## 2 DATA SAMPLING

The optical observations we model here were taken at the 3.5 m telescope in Calar Alto on the night of the 10th of October 2007. We used the lens array (LARR), made out of  $16 \times 16$  square elements, with the magnification scale of  $1 \times 1\ \text{arcsec}^2$ . The small field of view of LARR in this configuration does not cover the total surface of the region, thus a mosaic of 13 tiles was needed in order to map the whole area. The V300 grating provides us with relatively low spectral resolution ( $3.40\ \text{\AA}\ \text{pix}^{-1}$ ) but allows to cover the optical spectral range (3650–6990  $\text{\AA}$ ) we need for our modeling. Further details of the observations and data reduction can be found in Relaño et al. (2010).

The IR data of NGC 595 analyzed in this paper were

taken from the Spitzer Data Archive: the  $8\ \mu\text{m}$  image from IRAC (Infrared Array Camera, Fazio et al. 2004) and  $24\ \mu\text{m}$  -  $170\ \mu\text{m}$  from MIPS (Multiband Imaging Photometer, Rieke et al. 2004). The spatial resolutions of the images at 8, 24, 70, and  $160\ \mu\text{m}$  are  $\sim 2$ ,  $\sim 6$ ,  $\sim 18$  and  $\sim 40\ \text{arcsec}$ , respectively. The stellar contribution of the  $8\ \mu\text{m}$  image was subtracted using the emission at  $3.6\ \mu\text{m}$ , following the method described in Helou et al. (2004) and Calzetti et al. (2007). The IR observations and data reduction are explained in Relaño & Kennicutt (2009) for  $8\ \mu\text{m}$  and  $24\ \mu\text{m}$ , and in Verley et al. (2007) for the  $70\ \mu\text{m}$  and  $160\ \mu\text{m}$ .

The power of the IFS observations is based on the coverage of the whole face of the region, which allows us to extract not only spectral but also spatial information of NGC 595. Given the H $\alpha$  shell morphology of this particular H II region, we decided to extract spectra in elliptical concentric annuli covering the most intense zones of NGC 595 following this geometry. The spatial configuration of the elliptical annuli are depicted in Figure 1. The ellipses are all centered at the location of the main stellar clusters, (R.A. (J2000): 1h 33m 33.63s, DEC(J2000): 30d 41 m 32.6s), marked in the figure as a black star. The major to minor axis ratio of the ellipse is derived using the inclination angle of the galaxy ( $i=56^\circ$  for M33, van den Bergh, 2000), and we choose a position angle of  $129^\circ$  for the major axis since this orientation better traces the shell structure of the region (see Figure 1). In this configuration, we used rings of 2 arcsec width to obtain the elliptical profiles from our IFS observations. We restrict our models to the most intense parts of the region emitting at H $\alpha$ , which are covered by the ellipses depicted in Figure 1. The observed spatial configuration of this H II region makes it possible to perform the analysis in this way. Moreover, the mid-IR emission distributions at  $8\ \mu\text{m}$  and  $24\ \mu\text{m}$  are concentrated in this part of the region, therefore using the zone marked in Figure 1, we completely take them into account when performing the modeling.

We generated masks to isolate the emission coming from each annulus. These masks were then applied to the data cube of our IFS observations and integrated spectra for each annulus were produced. The spectra, covering 3650–6990  $\text{\AA}$ , were analyzed in the same way as explained in section 2.3 of Relaño et al. (2010). We used MPFITEXPR algorithm (Markwardt 2009) to fit the different emission lines with a Gaussian function plus a 1-degree polynomial function for the continuum subtraction. The final result of this procedure is a set of integrated fluxes for the emission lines fitted in the spectrum corresponding to each elliptical annulus. Flux errors were obtained as a combination of those derived in the profile fitting procedure and the uncertainty in the continuum subtraction (see Pérez-Montero & Díaz (2003) and references therein). Since the IFS observations were not taken under photometric conditions, no absolute calibration was performed, thus all the fluxes are in relative units. For the mid-IR bands, we use the same elliptical configuration as that used for IFS observations, but for the  $24\ \mu\text{m}$  observations we have chosen annuli of 6 arcsec width, similar to the angular resolution of the  $24\ \mu\text{m}$  image.

From the integrated emission line fluxes for each annulus we can then derive other parameters normally used to study the properties of the gas. In the top panels of Figure 2 we show the  $R_{23}$  parameter (left panel) ( $R_{23} = ([\text{O II}]\lambda 3727 + [\text{O III}]\lambda 4959,5007)/\text{H}\beta$ , Pagel et al. 1979) and

<sup>\*</sup> The adopted distance of M33 is 840 kpc (Freedman et al., 1991).

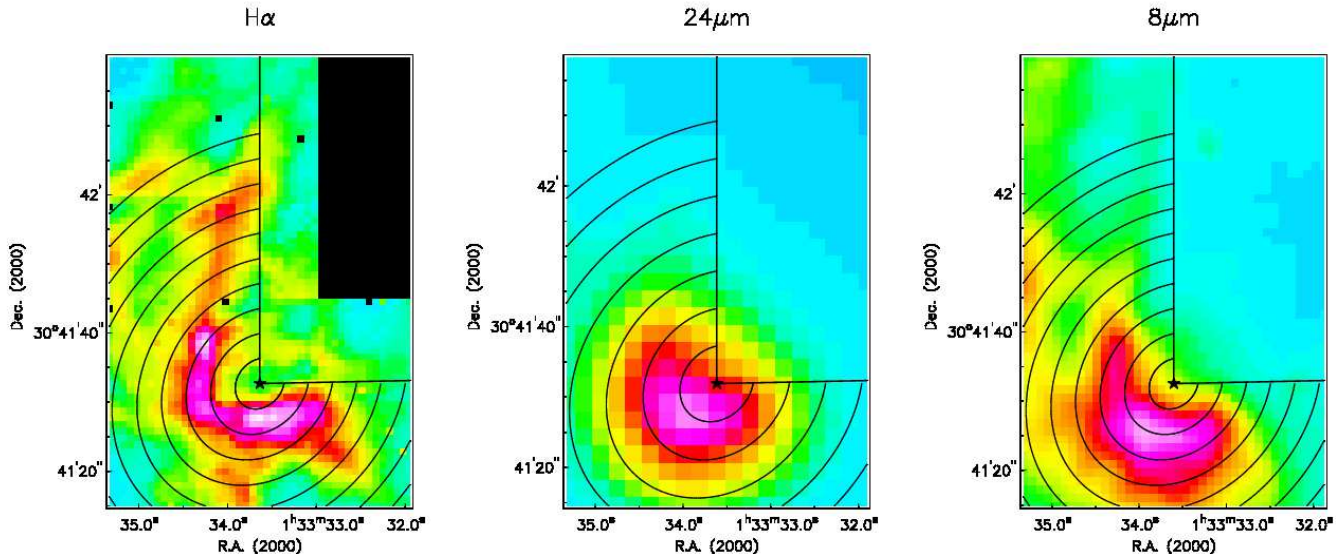


**Figure 1.** Left: map of the observed  $H\alpha$  flux derived from the IFS observations (Relaño et al. 2010). Center and right:  $24\ \mu\text{m}$  and  $8\ \mu\text{m}$  emission distributions, respectively. The elliptical annuli in the  $H\alpha$  and  $8\ \mu\text{m}$  images are separated by a distance of 4 arcsec projected onto the major axis of the ellipse (a separation of 2 arcsec was considered to obtain the integrated spectra for comparison to the models). In the case of the  $24\ \mu\text{m}$  the separation between annuli is 6 arcsec. The black star shows the location of the main stellar clusters (see text).

the  $[\text{O II}]/[\text{O III}]$  emission line ratio (right panel) as a function of the radial distance from the central stellar cluster.  $[\text{O II}]/[\text{O III}]$  changes over an order of magnitude: it shows low values closer to the location of the stars, indicating a high value of the ionization parameter, and rises towards larger distances from the stars where the ionization parameter declines. The  $R_{23}$  parameter, however, shows approximately the same value at any distance from the stellar cluster. This is indicative of the robustness of  $R_{23}$  to estimate the metallicity of H II regions (see Relaño et al. 2010). The  $H\alpha$  emission distribution normalized to the emission in the annulus with the largest collected flux (*i.e.* the fourth one, situated at  $\sim 7''$ ) is shown in the left-middle panel of Figure 2, revealing the  $H\alpha$  shell morphology of the region with a  $H\alpha$  maximum located at  $\sim 30$  pc from the stellar clusters (see also left panel of Figure 1). The IR profiles are shown in the center-right panel for the  $24\ \mu\text{m}$  emission and in the lower-left panel for the  $8\ \mu\text{m}$  emission, normalized to the emission of the annuli with largest emission in each case. Both 8 and  $24\ \mu\text{m}$  emission distributions show their maxima in a position outwards from the location of the stellar cluster (Figure 1). The lower-right panel shows the  $8\ \mu\text{m}/24\ \mu\text{m}$  radial profile at the spatial resolution of the  $24\ \mu\text{m}$  map. This ratio can be useful to study the nature of the dust, as  $8\ \mu\text{m}$  is expected to be mainly emitted by polycyclic aromatic hydrocarbons (PAHs) and it is then associated to the photodissociation region (PDR) or the diffuse ionized gas; while the emission at  $24\ \mu\text{m}$  is mainly due to the contribution of small dust grains at relatively high temperature. As we can see, there is an increase of the  $8\ \mu\text{m}/24\ \mu\text{m}$  ratio from 0.04 in the first annulus up to a maximum of  $\approx 0.4$  in a position much more outwards than the position of the maxima of the respective emissions in the  $8\ \mu\text{m}$  and  $24\ \mu\text{m}$  bands. Then it decreases slightly again. The trend observed here for the  $8\ \mu\text{m}/24\ \mu\text{m}$

shows that the hot dust emitting at  $24\ \mu\text{m}$  is partially mixed with the gas inside the H II region while in the outskirts of the region the emission at  $8\ \mu\text{m}$  becomes more prominent, probably as the emission from the PAHs becomes stronger, then it decreases again in the furthest annuli of the region.

## 2.1 Dust Mass and extinction in NGC 595

The mid-IR observations allow us to estimate the total amount of dust within the region and therefore obtain a measurement of the extinction that it produces. Then, we can compare the result with the extinction values obtained from the optical emission lines. We assume that most of dust mass is in the form of grains in thermal equilibrium, therefore the dust mass can be computed for a given flux ( $F_\nu$ ) using the following expression:

$$M_{\text{dust}} = F_\nu(T)D^2/\kappa_\nu B_\nu(T) \quad (1)$$

where  $F_\nu(T)$  is the observed flux,  $B_\nu(T)$  is the Planck function,  $\kappa_\nu$  is the mass absorption coefficient ( $\kappa_{100\ \mu\text{m}} = 63\ \text{cm}^2\text{g}^{-1}$ , (Lisenfeld et al., 2002), with  $\kappa_\nu \sim \nu^\beta$ ,  $\beta = 2$ , typical of interstellar grains (Draine & Lee 1984) and  $D$  is the distance of NGC 595. To derive the dust mass we need to know the temperature of the dust, which is normally estimated from the  $F(70\ \mu\text{m})/F(160\ \mu\text{m})$  ratio (e.g. Tabatabaei et al. 2007). Using the  $70\ \mu\text{m}$  and  $160\ \mu\text{m}$  images of M33 from Spitzer (Verley et al. 2007) we integrated the emission in these two bands for NGC 595 and estimate a temperature for the dust of  $\sim 30$  K. The result agrees with the values obtained by Tabatabaei et al. (2007) at the location of NGC 595 (see their fig.1) and is within the range of dust temperatures predicted recently by Kramer et al. (2010) for the central part of M33.

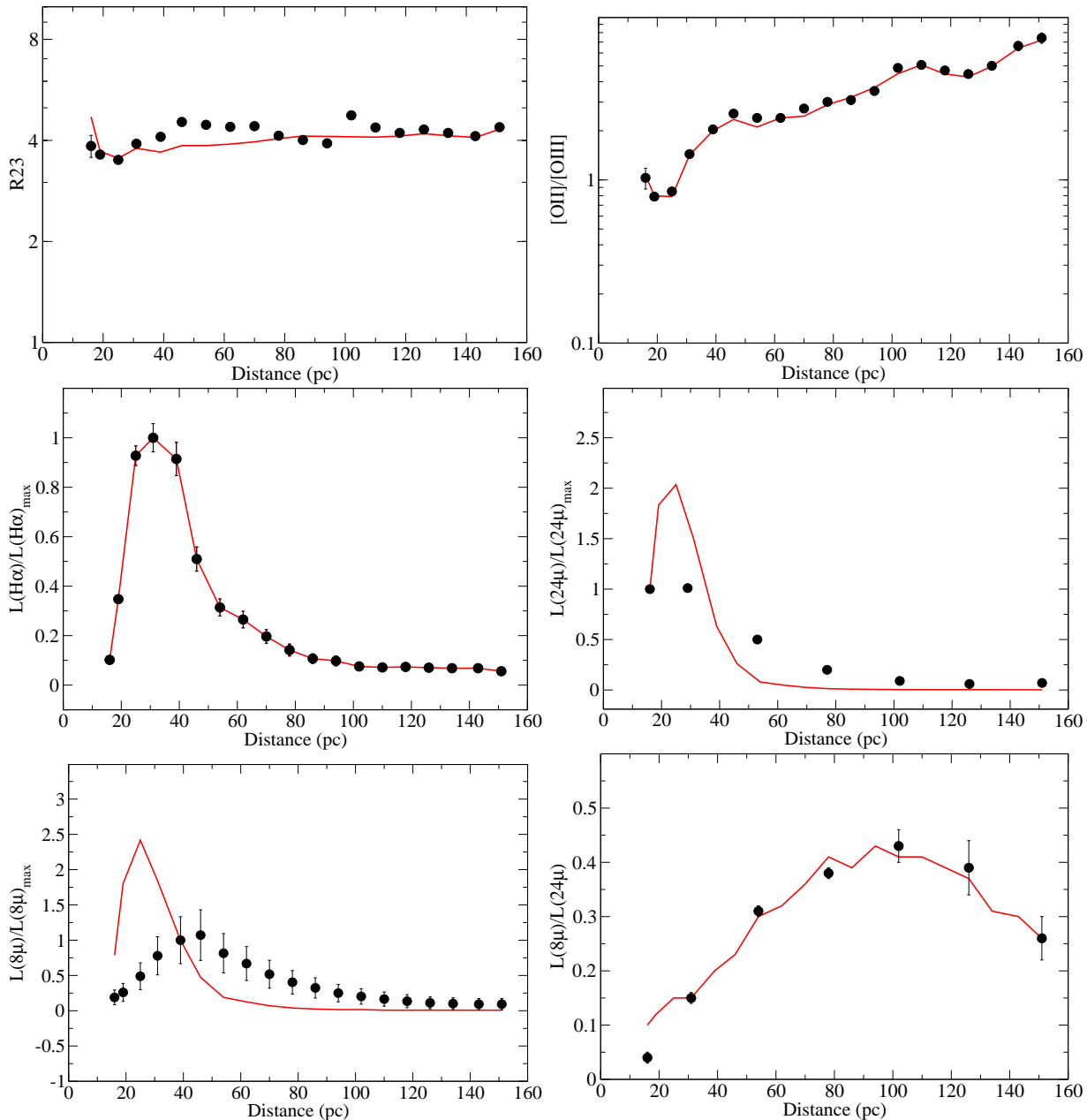


**Figure 2.** Radial profiles of some physical properties in NGC 595 as observed (in black circles) and as derived from the models (in red solid line).

Assuming a dust temperature of  $T=30$  K, we estimate the dust mass using the emission at  $160\mu\text{m}$  in Eq. 1. The result is  $M_{\text{dust}} = 1570 M_{\odot}$ , which agrees with the dust mass range predicted by Viallefond, Donas & Goss (1983). Taking into account the total gas mass of the region derived by Wilson & Scoville (1992),  $M(\text{HI}) + M(\text{H}_2) + M(\text{H}^+) \sim 1.3 \times 10^6 M_{\odot}$ , we obtain a dust-to-gas ratio for NGC 595 of  $\sim 1.2 \times 10^{-3}$ , a factor of  $\sim 6$  lower than the Galactic standard value ( $\sim 6.7 \times 10^{-3}$ , Draine & Lee 1984). Although this shows a significant discrepancy we note here that the metallicity of NGC 595 is  $\sim 0.6$  solar (Esteban et al. 2009), and therefore in principle we would expect a factor of two difference in the comparison of both dust-to-gas ratios. A possible reason for the relatively low dust-to-gas mass ratio might be the presence of cold dust not well traced

by the emission at  $160\mu\text{m}$ . In the case we only take into account the mass of ionized gas ( $2.3 \times 10^5 M_{\odot}$ , from the same reference), the ratio increases up to  $\sim 6.8 \times 10^{-3}$ .

We can also derive a measurement of the extinction that this amount of dust produces in the H II region. Using the dust temperature estimated above and the integrated flux at  $160\mu\text{m}$  for the H II region, we can predict the dust opacity at  $160\mu\text{m}$ ,  $\tau_{160\mu\text{m}}$ , following the equation:

$$\tau_{160} = F_{160}(T)/\Omega B_{160}(T) \quad (2)$$

where  $\Omega$  is the solid angle covered by the region. Assuming  $\tau_{160\mu\text{m}} \simeq 2200 \tau_{\text{H}\alpha}$  (Tabatabaei et al. 2007) we obtain an estimate of the extinction at H $\alpha$ . We derive  $\tau_{\text{H}\alpha} = 0.18$ , equivalent to  $A(\text{H}\alpha) = 1.086 \times \tau_{\text{H}\alpha} = 0.19$ . This value agrees within the uncertainties with the intrinsic extinction derived us-

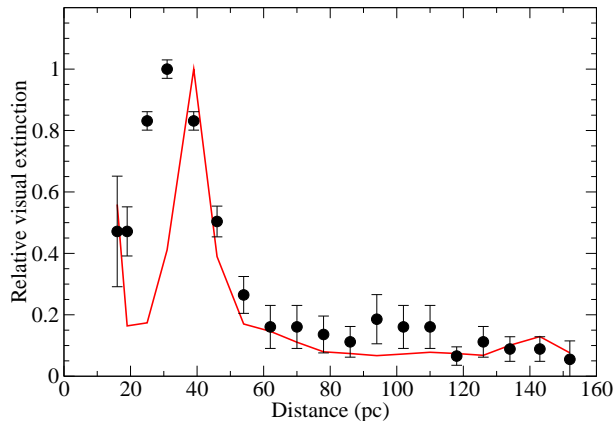


**Figure 3.** Radial profile of the observed (in black dots) and modeled (in red solid line) of the relative visual extinction. The normalization value is the maximum of each radial distribution.

ing the  $H\alpha/24\ \mu\text{m}$  ratio for NGC 595 (Relaño & Kennicutt, 2009) and it is very close (a difference of 0.08 mag) to the extinction value derived from the Balmer decrement using PMAS data (Relaño et al. 2010).

However, this extinction is not uniform across the nebula as it was already shown in Relaño et al. (2010). In Figure 3, we see in black dots the radial profile of the relative visual extinction normalized to the maximum value. The observed extinction variation within the H II region, which can be up to almost  $\sim 1$  mag, agrees with the extinction variation ( $\sim 1$ -1.5 mag) found by Viallefond et al. (1983) using radio continuum emission.

### 3 MODEL DESCRIPTION

Photoionization models were made to reproduce the observed properties in each annulus in both the optical and mid-infrared wavelength ranges. To do so, we resorted to the photoionization code CLOUDY v.08c (Ferland et al. 1998). This code allows the modelization of the effects of a radiation source situated in a determined spatial position on a one dimensional structure of gas and dust. Then, it can be extrapolated to a spherical close geometry or to an open geometry. Nevertheless, the open geometry assumption can not be applied in this case as the collected IFS data of NGC 595 do not provide the spatial distribution in the direction perpendicular to the plane of projection. An alternative procedure is to modelize each observed annulus with a single model of close geometry and to compare both the observed and modeled luminosities per unit of area (*i.e.* surface brightness) relative to the same luminosity in an arbitrary annulus. This procedure gives a qualitative rather than a quantitative analysis, but it constitutes a solid approach to study the variations of the physical properties of the gas as a function of the distance to the ionizing source in each annulus.

We chose for our analysis the Spectral Synthesis Population (SSP) spectra from the Starburst 99 libraries (Leitherer et al., 1999; Vázquez & Leitherer 2005), based on stellar atmosphere models from Smith et al. (2002), Geneva evolutionary tracks with high stellar mass loss (Meynet et al., 2004), a Kroupa Initial Mass Function (IMF; Kroupa

2002) in two intervals (0.1-0.5 and 0.5-100  $M_{\odot}$ ) with different exponents (1.3 and 2.3, respectively), the theoretical wind model (Leitherer et al. 1992) and a supernova cut-off of 8  $M_{\odot}$ . The selection of this IMF is justified by the detection of several supernova remnants in the proximity of this H II region (*e.g.* Gordon et al., 1995). The age of the ionizing burst was fixed to 4.5 Myr, according to the estimate made by Malumuth et al. (1996) using HST/WFPC-2 ultraviolet and optical resolved photometry. We fixed the metallicity of the stellar populations to  $Z = 0.02$  ( $= Z_{\odot}$ ), which is the closer value to the oxygen abundance measured by Esteban et al. (2009).

The modelization of each annulus was made independent to each other, assuming that each annulus has its own ionization structure originated at different distances from the same ionizing cluster. This gives a total of 19 photoionization models, one for each annulus, as defined in Section 2. We assumed different initial input model conditions for each of the defined annuli and then we followed an iterative method to fit the observed features, including the intensities of [OII] at 3727 Å and [OIII] at 4959 and 5007 Å emission lines relative to  $H\beta$  and the relative luminosity per unit of area of  $H\alpha$  and 8  $\mu\text{m}$  and 24  $\mu\text{m}$  Spitzer bands.

We considered the same input gas-phase metallicities in all the annuli as suggested by Relaño et al. (2010). This was set to match the value derived by Esteban et al. (2009), including He, O, N, S, Ne, Ar and Fe elemental abundances derived from optical collisionally excited lines and the measurement of the corresponding electron temperatures. The abundances for the rest of elements were rescaled taking as reference the difference to the oxygen abundance in the solar photosphere as done by Asplund et al. (2005). We assumed a constant density of 50 particles per  $\text{cm}^3$ , according to the values measured using the emission line ratio of [SII] (and which range between 10 and 100 particles per  $\text{cm}^3$  in the considered regions).

The inner radii of the ionized regions in each annulus can be initially estimated to reproduce the projected distances in the emission maps. Hence, the projected distance between the first annulus and the ionizing source is of 1" (corresponding to 4 pc at the assumed M33 distance). However, we considered a larger distance for this closest annulus in order to optimize the fitting of the observed quantities in the models. In this case, the best agreement between the observed and modeled emission line ratios is found assuming a distance of 16 pc between the inner face of the gas and the ionizing source. The difference between the distance found by the models and the projected distance observed for this annulus could be interpreted using a non-seen component of the distance in the direction perpendicular to the plane of projection. However, this deprojection is not required to find an agreement between models and observations in the furthest annuli. Therefore, the ratio between the adopted and projected distances is not maintained for all the other annuli, but it gradually decreases assuming the geometry of a hollow ellipsoid of revolution. Therefore, the considered factor of deprojection for the furthest annulus is 1 (*i.e.* the distance measured in the projected image and the inner radius of its corresponding model is the same, which is 151 pc in this region). In Figure 4 we show this geometry in a cut plane perpendicular to the plane of the projected sky. This plot also shows the adopted distances between the in-

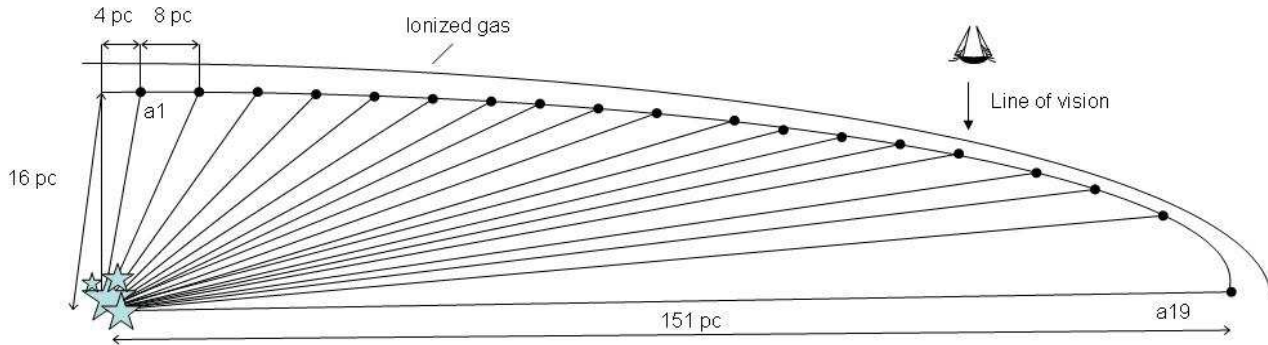


**Figure 4.** Schematic representation of the adopted geometry of each of the 19 linear models made to reproduce the observed features in each of the observed annuli of NGC 595. The line of vision indicates the orientation of the detectors to acquire the available observational information taken for our models. The schematic representation here shows the dimension above the plane of the sky of the annuli plotted in Figure 1.

ner face of the ionized gas and the ionizing stellar cluster in the models of each annulus.

We left as free parameters the filling factor, the thickness of the gas shell and the amount of dust, which vary in each iteration of the model in order to find the best agreement with the observed quantities. In all models filling factor and thickness lead to a plane-parallel matter bounded geometry, where a large fraction of the ionizing photons emitted by the central cluster escape to the outer interstellar medium of the galaxy. The dust-to-gas ratio is a fundamental component to reproduce the ionization structure of the gas because the dust heating affects its thermal balance. We assumed the default grain properties of CLOUDY v08.00c, which has, essentially, the properties of the interstellar medium and follows a MRN (Mathis, Rumpl & Norsieck 1997) grain size distribution.

#### 4 RESULTS AND DISCUSSION

In Figure 2 we show in solid red line the predictions made by the model for each annulus in comparison with the same observed properties. As these same properties were taken as input parameters in the models, the agreement in the most part of them is excellent. Hence, the  $R_{23}$  parameter is well traced by the models, as a consequence of the same adopted metallicity for all the considered annuli. Regarding the  $[\text{O II}]/[\text{O III}]$ , this ratio is well reproduced across all the structure as a consequence of the ionization parameter decrease, which varies in the models from  $\log U = -2.91$  in annulus 1 to  $\log U = -3.49$  in annulus 19. Other optical lines than  $[\text{O II}]$  or  $[\text{O III}]$  can trace both the metallicity and ionization parameter across the region, as it is the case of the sulphur emission lines  $[\text{S II}]$  at 6717, 6731 Å and  $[\text{S III}]$  at 9069, 9532 Å. In upper-left panel of Figure 5, we see the variation of the  $S_{23}$  parameter, defined as the intensity sum of  $[\text{S II}]$  and  $[\text{S III}]$  relative to  $\text{H}\beta$  (Vílchez & Esteban, 1996), which is sensitive to the metal content of the gas in a wide range of metallicity (Díaz & Pérez-Montero, 2000). As we can see, the rate of variation is quite similar to that observed in  $R_{23}$  ( $\approx 20\%$ ). Regarding the ionization parameter the ratio of these sulphur emission lines,  $[\text{S II}]/[\text{S III}]$ , can also trace the decrease in the ionization degree of the nebula

(Díaz, 1988) following the same trend as  $[\text{O II}]/[\text{O III}]$ , as we can see in the upper-right panel of Figure 5. This indicates that sulphur lines supply an alternative in the red part of the optical spectrum to oxygen emission lines in the blue to derive the ionization state and the metal content of ionized gaseous nebulae.

Despite of the dependence of both, oxygen and sulphur, emission line ratios on the ionization parameter, as the ionization potentials of the involved oxygen and sulphur ions are close, the quotient between these two ratios cancels its dependence on ionization to first order parameter, keeping a certain dependence on the shape of the ionizing stellar source (*i.e.* the equivalent effective temperature, Vilchez & Pagel, 1988). This quotient is defined as the  $\eta'$  parameter:

$$\eta' = \frac{[\text{O II}]/[\text{O III}]}{[\text{S II}]/[\text{S III}]} \quad (3)$$

which increases for lower stellar effective temperatures. The corresponding  $\eta$  parameter is also similar but it depends on the relative ionic abundance ratios. For this case, as no chemical inhomogeneities were detected, the two indicators are expected to behave in similar manners. However, as we can see in middle-left panel of Figure 5, although we used the same stellar synthetic atmosphere in all models, this parameter increases from the inner to the outer annuli in almost an order of magnitude, showing a big jump of 0.75 dex in the central 40 pc (*i.e.* the location of the  $\text{H}\alpha$  shell). This indicator, defined originally for integrated observations of giant  $\text{H II}$  regions, must be considered carefully in gas shells and matter-bounded geometry when studying the spatial variations of the effective temperature across a region with IFS data.

The relative surface brightness of  $\text{H}\alpha$  in each model is also well reproduced, with a maximum of this emission in the annulus 4, identical as derived from the PMAS IFU observations. The two most important input parameters in the models controlling this relative emission across the nebula are the filling factor ( $\epsilon$ ) and the thickness of the shell in each matter-bounded model. As it is possible in models to increase the relative emission of the Balmer emission lines by both increasing these two parameters, it is not possible with these data to break the degeneracy of them and it is necessary to define a parameter which allows a direct com-

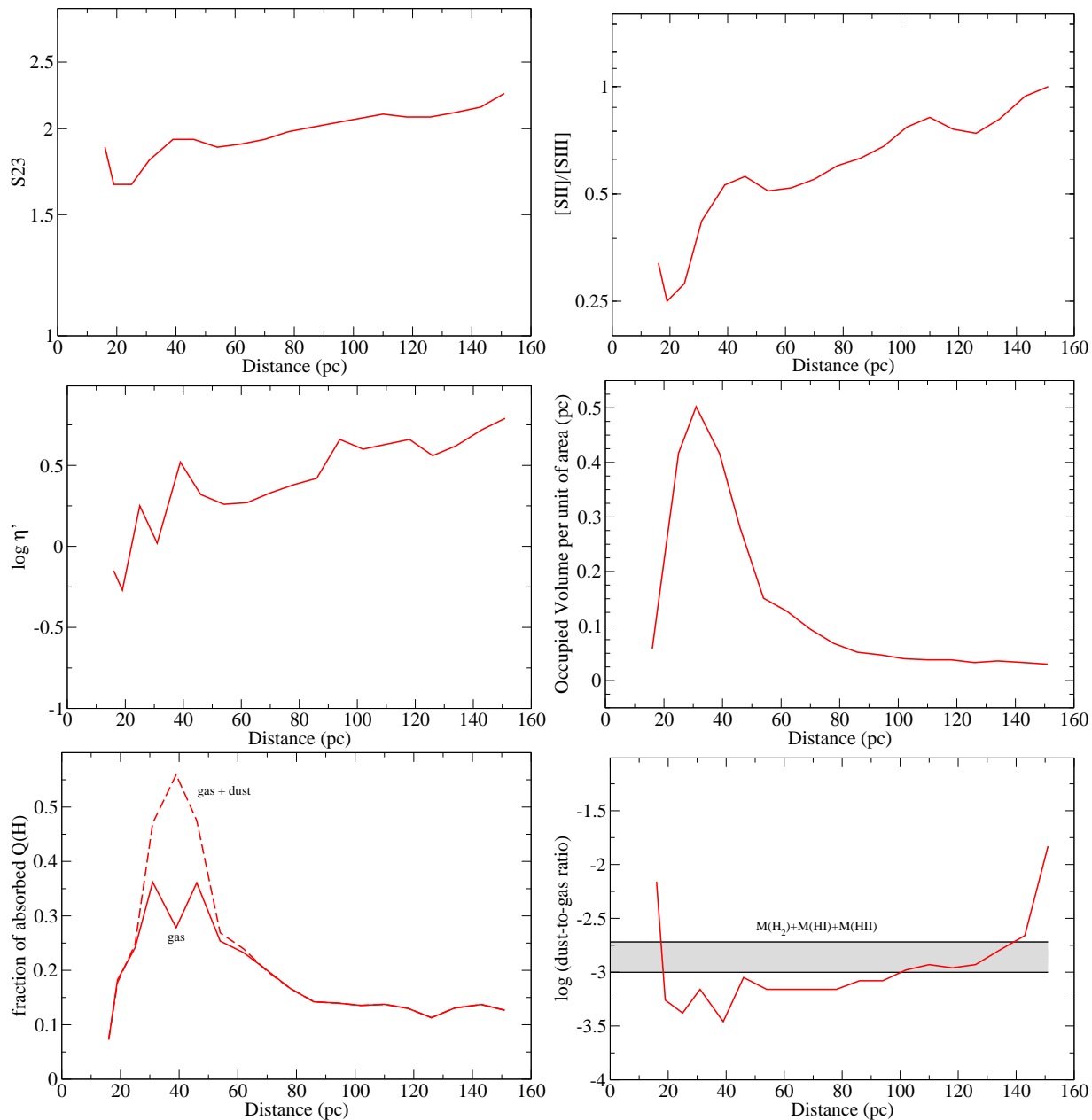


**Figure 5.** Radial profiles of some physical properties as predicted by the models (in red solid line). See the text for details.

parison between the input conditions of each model. In this way, we can define the occupied volume ( $V_o$ ), as:

$$V_o = \epsilon \times V(r_i, r_o) \quad (4)$$

where  $\epsilon$  is the filling factor and  $V$  is the total volume of the gas in a thin shell, hence depending on inner and outer radius of each annulus. In the middle-right panel of Figure 5 we show the variation of the occupied volume for each annulus. The maximum in the relative emission of  $H\alpha$  matches with a maximum in the occupied volume, which is in turn due to a possible increase of the filling factor or the thickness of the nebula in these positions.

Regarding the infrared, the emission of the nebula predicted by the models in the  $8\mu\text{m}$  and  $24\mu\text{m}$  Spitzer bands were derived by subtracting the incident to the transmitted continuum in each model to remove the stellar contribution.

Then we convolved the resulting spectrum with the shape of the corresponding Spitzer filters. As in the case of the  $H\alpha$  emission, as models were calculated in a close spherical geometry, only surface brightness were compared to the observations. As it can be seen in the middle-right and lower-left panels of Figure 2, the radial profiles of the relative emission of both  $8\mu\text{m}$  and  $24\mu\text{m}$  are reproduced by the models up to some extent, with a larger relative emission of both maxima in the models. Besides, the position of the maximum in the  $8\mu\text{m}$  panel is predicted by the models in a position slightly closer to the cluster than in the observations.

Nevertheless, by varying the dust-to-gas ratio in each model the  $8\mu\text{m}/24\mu\text{m}$  ratio was perfectly fitted. The measured values of this ratio across the nebula range from 0.04 in the inner regions to a maximum of about 0.4 at 100 pc, but it decreases again at further positions. This decrease is

explained by the models by an enhancement of the dust-to-gas ratio in these positions. The values of the  $8\ \mu\text{m}/24\ \mu\text{m}$  ratio measured in NGC 595 are lower in all cases than the average values measured by Bendo et al. (2008) for a sample of nearby spiral galaxies. These authors point out that in this sample the PAHs in the diffuse cold gas are expected to be responsible for most of the  $8\ \mu\text{m}$  emission. As our models predict that NGC 595 is a matter-bounded shell with no PDR, no PAHs are expected to appear and the emission at the  $8\ \mu\text{m}$  is emission mainly dominated by the IR continuum emitted by gas and dust at this wavelength. On the other hand, the  $24\ \mu\text{m}$  emission is high in this region due to the fraction of small hot dust grains surviving in the ionized gas. These grains are also responsible for the absorption of a non-negligible fraction of the ionizing photons. In lower-left panel of Figure 5 we see the fraction of these photons (i.e. with an energy larger than 13.6 eV) absorbed both by the gas (in red solid line) and by the gas and the dust (in dashed red line). The most part of these photons escape from the gas shell in those annuli with a lower occupied volume (i.e. with a lower filling factor or a lower thickness), and the relative fraction of absorbed photons by dust is almost negligible. However, in those regions whose occupied volume increases to fit the relative emission of  $\text{H}\alpha$ , the fraction of absorbed photons, which is more than a half here, is due similarly to gas and dust. This is due to a larger fraction of bigger dust grains, that survive at further distances, also enhancing the emission at  $24\ \mu\text{m}$ . This also affect the relative visual extinction due to the dust grains in each annulus. In Figure 3, we see the comparison between the relative visual extinction derived from the Balmer decrement in each annulus as compared to the values predicted by the models. The models fit fairly well the pattern of variation with a maximum of the extinction in the same annulus of the fraction of occupied volume and, hence, the fraction of absorbed ionizing photons is larger. This same region corresponds to the maximum in the relative emission at  $24\ \mu\text{m}$ .

Finally, in the lower-right panel of Figure 5 we show the dust-to-gas ratio obtained to fit the  $8\ \mu\text{m}/24\ \mu\text{m}$  ratio. This is relatively constant for the most part of the annuli in a value about  $10^{-3.2} = 6.3 \times 10^{-4}$ , with the exception of the first annulus, where it is of  $10^{-2}$  and in the the last two annuli, where it also increases. These values are within the range of estimates made for the dust mass in the region based on the IR bands from Spitzer (see subsection 2.1).

## 5 SUMMARY AND CONCLUSIONS

We carried out a set of photoionization models to describe the spatial distribution of the optical and mid-IR properties of NGC 595, the second most luminous H II region in the disk of the spiral galaxy M33. These models reproduce for the first time and simultaneously the spatial radial profile of several observed properties in both the optical and the mid-IR. We used the Integral Field Spectroscopy observations in the optical spectral range from the PMAS instrument in the CAHA 3.5 m telescope (see Relaño et al. 2010) and the maps of  $8\ \mu\text{m}$  and  $24\ \mu\text{m}$  taken by the Spitzer telescope. The input conditions extracted from the sets of spatially resolved observations were divided in elliptical annular regions around the central position of the H II region, occupied by the ion-

izing stellar cluster. Then, we derived the spatial profiles of the  $\text{H}\alpha$ ,  $8\ \mu\text{m}$  and  $24\ \mu\text{m}$ , relative surface brightness, the relative [O II] and [O III] emission line intensities and the extinction variation across the region. We also took as input conditions of our models the gas metallicity reported by Esteban et al. (2009;  $12+\log(\text{O}/\text{H}) = 8.45$ ) and the age of the central stellar cluster, 4.5 Myr, derived by Malumuth et al. (1996).

This information was taken into account in the photoionization code CLOUDY v. 08.00c (Ferland et al. 1998), assuming that each analyzed annulus can be considered as an independent H II structure. The distance between the inner radius of the gas shell and the central cluster was set to fit the projected measured distance of each annulus but taking into account a certain deprojection factor in the case of the closest annuli. Since no information about the distribution of the gas and the dust in the axis perpendicular to the plane of projection can be collected, we considered spherical closed shells of gas in our models and then we varied the filling factor, the shell thickness and the dust-to-gas ratio in an iterative method in order to fit the corresponding surface brightness and relative variations of the observed properties.

Our models reproduce fairly well the uniformity of the  $R_{23}$  parameter, indicative of an homogeneous metal content across the nebula, and the increase of the [O II]/[O III] ratio, as a consequence of the decrease of the ionization parameter. They also indicate that the same parameters based on sulphur emission lines (i.e. [S II] and [S III]) are also valid to trace these variations across the radial distribution of the H II region. Nevertheless a more accurate analysis of the spatial variation of the metal content of this nebula could be carried out with the corresponding maps of the electron temperature. However, despite of a single common ionizing source, models indicate a  $\sim 1$  dex variation of the  $\eta'$  parameter (Vílchez & Pagel 1988), which is related to the equivalent effective temperature of the ionizing source. This result indicates that this parameter must be used with care for the study of the spatial variations of the ionizing field in H II regions which are matter-bounded or present a complex geometry.

Our models also reproduce the variation of the  $\text{H}\alpha$  surface brightness, which peaks at a distance of about 30 pc and decreases at further distances. According to the models, this variation is due to the combination of a matter-bounded geometry of the gas shell in all annuli and the variation of the occupied volume across the shell. The occupied volume depends on the filling factor and the thickness of the shell, but our models are not able to distinguish between these two parameters to explain the enhancement in the  $\text{H}\alpha$  emission. According to these models, the number of ionizing photons escaping from the nebula varies between a 45% in the maximum of occupied volume and about a 90% in the furthest annuli.

Although the  $8\ \mu\text{m}$  is not well reproduced, the  $8\ \mu\text{m}/24\ \mu\text{m}$  ratio fits fairly well with the predictions of our models. This ratio, which varies between 0.04 at the closest annulus and peaks at 0.4 in the outskirts of the nebula, is much lower than the values measured by Bendo et al. (2008) in radial profiles of spiral galactic disks. As models predict that all annuli are matter bounded and hence no photodissociation region is formed at close distances of the ionizing source, the PAHs dominating the  $8\ \mu\text{m}$  emission are much



weaker than in the diffuse cold gas regions of those galaxies. On the other hand, as  $24\ \mu\text{m}$  emission is mainly due to small hot grains surviving in the ionized gas, the  $8\ \mu\text{m}/24\ \mu\text{m}$  ratio is low in all the modeled annuli.

The geometrical variation of the occupied volume across the region also shows some implications in the extinction structure of the region. Therefore, as the number of hydrogen ionizing photons absorbed by the dust is only increased in the regions with a larger occupied volume, the extinction also increases in the same region, according to the PMAS observations. Regarding the dust-to-gas ratio, models predict values compatible with the estimates made using the gas mass from Wilson & Scoville (1992) and the dust mass derived from the integrated 70 and  $160\ \mu\text{m}$  bands from Spitzer. The dust-to-gas ratio estimated for the whole region ( $\sim 1.2 \times 10^{-3}$ ) is lower than in the Solar Neighbourhood, but consistent if we take into account that the metal content of this H II region is subsolar. In this sense, the corresponding spatial distribution of the emission at  $70\ \mu\text{m}$  and  $160\ \mu\text{m}$  would supply the spatial distribution of the dust-to-gas ratio to be directly compared with the results from the models presented in this work but the spatial resolution up to now does not allow to perform this study. Future observations from Herschel telescope will be unique to address this issue.

## ACKNOWLEDGEMENTS

This work has been supported by the projects AYA2007-67965-C03-02 of the Spanish National Plan for Astronomy and Astrophysics and CSD2006 00070 "1st Science with GTC" of the Spanish Ministry of Science and Innovation (MICINN). This research was also supported by a Marie Curie Intra European Fellowship within the 7<sup>th</sup> European Community Framework Programme. We would like to thank Simon Verley for kindly providing us with the SPITZER  $70\ \mu\text{m}$  and  $160\ \mu\text{m}$  images, to David Martín-Gordón for his help with the convolution of synthetic spectra and Spitzer filters and to Ute Lisenfeld for very helpful discussions. This work is based in part on observations made with the Spitzer Space Telescope, which is operated by the Jet Propulsion Laboratory, California Institute of Technology under a contract with NASA.

## REFERENCES

- Bendo, G. J., et al. 2008, MNRAS, 389, 629  
 Calzetti, D., et al. 2007, ApJ, 666, 870  
 Díaz, A. I., 1988, MNRAS, 231, 57  
 Díaz, A. I., & Pérez-Montero, E. 2000, MNRAS, 312, 130  
 Draine, B. T. & Lee, H. M. 1984, ApJ, 285, 89  
 Drissen L., Crowther P. A., Úbeda L., Martín, P. 2008, MNRAS, 389, 1033  
 Esteban C., Bresolin F., Peimbert M., García-Rojas, J., Peimbert, A., Mesa-Delgado, A. 2009, ApJ, 700, 654  
 Ercolano B., Bastian N., Stasińska G., 2007, MNRAS, 379, 945  
 Fazio, G. G., et al. 2004, ApJS, 154, 10  
 Freedman W. L., Wilson C. D., Madore B. F., 1991, ApJ, 372, 455  
 Gordon, S. M., Kirshner, R. P., Long, K. S., Blair, W. P., Duric, N., & Smith, R. C. 1998, ApJS, 117, 89  
 Helou, G., et al. 2004, ApJS, 154, 253  
 Kramer, C. et al. 2010, A&A, astro-ph1005.2563  
 Le Fèvre, O., et al. 2003, SPIE, 4841, 1670  
 Lisenfeld, U., Israel, F. P., Stil, J. M., Sievers, A. 2002, A&A, 382, 860  
 Markwardt C. B. 2009, PASP, 411, 251  
 Malumuth E. M., Waller W. H., Parker J. W., 1996, AJ, 111, 1128  
 Pagel B. E. J., Edmunds M. G., Blackwell D. E., Chun, M. S., Smith, G. 1979, MNRAS, 189, 95  
 Pellerin A., 2006, AJ, 131, 849  
 Pérez-Montero, E., & Díaz, A. I. 2003, MNRAS, 346, 105  
 Relaño, M. & Kennicutt, R. C. Jr. 2009, ApJ, 699, 1125  
 Relaño, M., Monreal-Ibero, A., Vílchez, J. M., Kennicutt, R. C. 2010, MNRAS, 402, 1635  
 Rieke, G. H., et al. 2004, ApJS, 154, 25  
 Tabatabaei, F. S., Beck, R., Krügel, E., Krause, M., Berkhuijsen, E. M., Gordon, K. D., Menten, K. M. 2007, A&A, 475, 133  
 Sánchez S. F., Cardiel N., Verheijen M. A. W., Martín-Gordón, D., Vílchez, J. M., Alves, J. 2007, A&A, 465, 207  
 van den Bergh S. 2000, The galaxies of the Local Group, Cambridge University Press, Cambridge, UK  
 Verley, S., Hunt, L. K., Corbelli, E., Giovanardi, C. 2007, A&A, 476, 1161  
 Vilchez, J. M., & Esteban, C. 1996, MNRAS, 280, 720  
 Vilchez, J. M., & Pagel, B. E. J. 1988, MNRAS, 231, 257  
 Vílchez, J. M., Pagel, B. E. J., Díaz, A. I., Terlevich, E., Edmunds, M. G. 1988, MNRAS, 235, 633  
 Viallefond, F., Donas, J. & Goss, M. 1983, A&A, 119, 185  
 Wilson, C. & Scoville, N. 1992, ApJ, 385, 512  
 Wood, K., Mathis, J. S., & Ercolano, B. 2004, MNRAS, 348, 1337